Time domain numerical simulation of elastic plate subjected to turbulent boundary layer wall-pressure fluctuations

S. Anantharamu[1] and K. Mahesh[1]

([1]Department of Aerospace Engineering & Mechanics, University of Minnesota, USA)

ABSTRACT

We numerically obtain the time-domain response of an elastic plate subjected to turbulent boundary layer wall-pressure fluctuations at two $Re_\tau = \frac{u_\tau \delta}{\nu}$ where u_τ is the friction velocity, δ is the characteristic length scale and ν is the kinematic viscosity. Two datasets of turbulent boundary layer wall-pressure fluctuations are considered: synthetically generated time-domain wall-pressure fluctuations at Re_τ=2223, and Direct Numerical Simulation (DNS) wall-pressure fluctuations generated at Re_τ=180. For the first dataset, wall-pressure fluctuations are generated using the Corcos cross-spectral density and Smolyakov-Tkachenko auto-spectral density model. A time-domain algorithm to synthetically generate the wall-pressure fluctuations comprising of 1 billion wavenumbers/frequencies from a prescribed wavenumber-frequency spectrum and, efficient and accurate computation of forces on finite element mesh using L^2-orthogonal projection is developed. The numerically obtained velocity response at a point on the plate shows good agreement with the experimental result of Han et al. (1999). For the second dataset, wall-pressure fluctuations are generated by performing DNS of turbulent channel flow at $Re_\tau = 180$. A load transfer algorithm to accurately transfer the piecewise constant load present in the fine fluid surface mesh to a coarse solid surface mesh is discussed where the fine fluid surface mesh is assumed to be embedded in the coarse solid surface mesh. The plate response using DNS wall-pressure fluctuations is obtained for steel and POM (polyoxymethylene) polyacetate plates, with clamped boundary conditions and compared.

INTRODUCTION

The excitation of solid structures by turbulent flow influences the radiated far-field sound. A flat-plate turbulent boundary layer is a canonical example of such interaction. Willmarth and Wooldridge (1962), Corcos (1964), Bull (1967), Blake (1970), Farabee and Casarella

(1991), Ciappi et al. (2009) performed measurements of wall-pressure fluctuations, including root-mean-square (rms) fluctuations, power spectral density, longitudinal and lateral cross-correlation and spectral density and convection velocity beneath turbulent boundary layers. An interesting result of Farabee and Casarella (1991) is the scaling of auto-spectral density of wall pressure fluctuations. They classified the frequency range into low $\left(\frac{\omega\delta}{u_\tau} < 5\right)$, mid $\left(5 < \frac{\omega\delta}{u_\tau} < 10\right)$, overlap (for sufficiently high Re_τ)$\left(100 < \frac{\omega\delta}{u_\tau} < 0.3Re_\tau\right)$ and high $\left(\frac{\omega\delta}{u_\tau} > 0.3Re_\tau\right)$. Scaling quantities which led to collapse of auto-spectral density for different Re_τ for each of the frequency ranges were identified through which the location of source that contributes the most to the frequency range was discerned. Willmarth (1975), Bull (1996) and Blake (2017) have published comprehensive reviews of wall-pressure fluctuations.

Kim (1989) computed power spectra, probability density function and two-point correlations of wall-pressure fluctuations from turbulent channel flow DNS at $Re_\tau = 180$ of Kim et al. (1987). Choi and Moin (1990) computed wavenumber-frequency spectra and frequency dependent convection velocity of wall-pressure at $Re_\tau = 180$ from the DNS dataset of Kim et al. (1987). Hu et al. (2006) computed wall-pressure spectra and rms values of wall-pressure in turbulent channel flow upto Re_τ of 1440 using DNS. Sillero et al. (2013) performed DNS of turbulent boundary layers and computed rms wall pressure for Re_τ up to 2000. A common finding of the DNS of Hu et al. (2006) and Sillero et al. (2013) is that the rms wall pressure varies with the logarithm of Re_τ. This is exactly the contribution of the overlap region which dominates for higher Re_τ as evaluated by Farabee and Casarella (1991), assuming ω^{-1} dependency of the wall-pressure spectrum in the overlap region based on the work of Panton and Linebarger (1974). Effects of adverse pressure gradient on wall-pressure fluctuations in a turbulent boundary layer were studied using DNS

by Na and Moin (1998). Due to the computational cost of performing DNS to generate accurate data of wall-pressure fluctuations, alternative methods to model wall-pressure fluctuation spectrum based on the Reynolds averaged Navier-Stokes equations have been proposed by Lee et al. (2005), Peltier and Hambric (2007) and Hu et al. (2017).

Smol'Iakov and Tkachenko (1991), Bull (1967), Goody (2004) and several others have proposed wall-pressure auto-spectral density models based on experimental measurements. Hwang et al. (2009) reviewed nine wall-pressure spectrum models and compared them to various experimental data over a wide range of Reynolds numbers. Corcos (1964), Chase (1980), Hwang (1998), Caiazzo and Desmet (2016) and several others have proposed cross-spectral density models. Graham (1997) compared several cross-spectral density models for the sound power radiated by plates. The experiments of Willmarth and Wooldridge (1962) observed that assuming Taylor hypothesis, the ratio of contribution of a particular wavenumber $\left(k = \frac{\omega}{U_c}\right)$ (where U_c is the convection velocity/speed of moving frame of reference) to auto-correlation in a moving reference frame is dependent only on $\frac{\omega x_1}{U_c}$ (where $x_1 = U_c \tau$ and τ is the time lag in the auto-correlation. This is the distance travelled by the moving frame during the time τ). Willmarth and Wooldridge (1962) observed this to be an indication that the contribution of eddies of wavenumber k to cross-correlation decays by a constant fraction after travelling distances proportional to their wavelength. Corcos (1964) used these heuristics along with experimental data of pipe flow to propose the following form of the cross-spectral density of wall-pressure:

$$R_{pp}(\zeta_1, \zeta_2, \omega) = R_{pp}(0, 0, \omega) A\left(\frac{\zeta_1 \omega}{U_c}\right) B\left(\frac{\zeta_2 \omega}{U_c}\right) e^{-i\frac{\omega \zeta_1}{U_c}}$$
(1)

where ζ_1, ζ_2 are the streamwise and spanwise separation respectively, $A\left(\frac{\zeta_1 \omega}{U_c}\right)$ and $B\left(\frac{\zeta_2 \omega}{U_c}\right)$ represent the decay of cross-spectral density with increasing streamwise and spanwise separation respectively, U_c is the convection velocity. Different Corcos type models have different forms of the function $A\left(\frac{\zeta_1 \omega}{U_c}\right)$ and $B\left(\frac{\zeta_2 \omega}{U_c}\right)$.

Theoretical frequency domain methods using modal superposition and Poisson-Kirchoff plate theory response from a given cross-spectral density model of wall-pressure fluctuation have been discussed by Elishakoff (1983) and Blake (2017). Hwang and Maidanik (1990) computed modal sensitivity function for rectangular and circular panel with simply supported, clamped and free boundary conditions. Frequency-domain Finite Element Methods (FEM)

have been used by Hambric et al. (2004) to obtain cross-spectral density of structural response from a given cross-spectral density of surface pressure. They compare the velocity power spectral density at a point on the plate with the experiments of Han et al. (1999) using model cross-spectral density spectrum of wall-pressure. We use the same experiment of Han et al. (1999) to verify our time-domain plate response to synthethically generated wall-pressure fluctuations at $Re_\tau = 2233$. Hambric et al. (2004) observed that the wavenumber transform of clamped mode shape overlaps mainly with the low wavenumber region of wall-pressure wavenumber frequency spectrum whereas that of mode shape with free boundary condition, significantly overlaps with the convective peak of wall-pressure wavenumber frequency spectrum for a large range of frequencies. So, they proposed two models which separately approximated the low-wavenumber region and the convective component of the modified Corcos model of Hwang (1998). The proposed models were compared to response of plates obtained from FEM using the modified Corcos model for different plate thickness, loss factor and boundary conditions. Scaling laws for mean power spectral density of response of thin plates have been proposed by Ciappi et al. (2012, 2015). They compared the collapse of several experimental measurements of the mean plate response for different scaling variables.

Large Eddy Simulation (LES) is increasingly used to compute complex turbulent flows (Mahesh et al., 2015). LES propeller crashback calculations of pressure on the blade surface was used to obtain response and stresses in the blade for two advance ratios by Chang et al. (2008). Hambric et al. (2015) used pressure fluctuations generated by LES simulation of a turbulent shear layer from a nozzle to excite a simply supported beam placed at the nozzle exit and assessed potential structural damage. Schäfer et al. (2010) used coupled LES flow, structure and acoustics solvers to obtain the radiated acoustic pressure from a flexible plate adjacent to a turbulent boundary layer in the far field. The quantitative values of sound pressure level spectra differed significantly between the measured and numerically predicted values due to higher damping values of the plate in the experimental setup than in the numerical simulation.

In this paper, we consider time-domain simulation of plate response to wall-pressure fluctuations. We first discuss the development and validation of the parallel FEM solver. This is followed by a description of the methodology used to generate synthetic wall-pressure fluctuations from a given wavenumber frequency spectrum, and load transfer strategy for surface pressure for efficient and accurate computation of the loads on the structure. Then, we discuss the details of the DNS used to generate wall-pressure fluctuations at

$Re_\tau = 180$ and present a load-transfer strategy. The response of a steel plate subjected to the wall-pressure fluctuations representative of the Han et al. (1999) experiment is then discussed and velocity spectra at a point on the plate are compared to the experiment. This is followed by the DNS results for turbulent channel flow, and comparison of response of steel and POM polyacetate material at $Re_\tau = 180$.

PARALLEL LINEAR ELASTICITY STRUCTURAL SOLVER

We briefly discuss the numerical details of the finite element methodology used to solve the dynamic linear elasticity equations. This is followed by a discussion of the solver and its validation.

Numerical Method

The governing equations for dynamic linear elasticity are the momentum conservation equations (summation implied on repeated indices)

$$\rho^s \frac{\partial^2 d_i^s(\mathbf{x},t)}{\partial t^2} = \frac{\partial \sigma_{ij}^s(\mathbf{x},t)}{\partial x_j} + f_i(\mathbf{x},t), \quad (2)$$

where $\mathbf{x}$ is the location in the solid domain, t is the time, ρ^s is the solid density, d_i^s is the solid displacement vector component , σ_{ij}^s is the solid stress tensor and f_i is the component of body force. A linear constitutive law is assumed for the stress tensor σ_{ij}^s. Eq. 2 is referred to as the strong form of the governing equations. The above equation is converted to weak (Hughes, 2012) form by multiplying with a test function and requiring solutions that are continuous which may not have pointwise classical derivatives (Brenner and Scott, 2007). Then, an approximate solution is obtained from the Galerkin formulation, by choosing the approximate solution and the test function as a linear combination of a finite set of basis functions in the weak formulation.

On choosing Lagrange polynomials as the basis of the approximate solution, we obtain

$$M\ddot{\mathbf{d}}(t) + K\mathbf{d}(t) = \mathbf{f}(t), \quad (3)$$

where M is the mass matrix, K is the stiffness matrix, $d(t)$ is the displacement and $f(t)$ is the force vector on the degrees of freedom at the nodes at time t. To incorporate damping in the structure, the Rayleigh damping model is used, i.e. the damping matrix C is approximated as

$$C = \alpha M + \beta K, \quad (4)$$

where α and β are mass and stiffness proportional damping constants respectively. The system of ODEs in Eq. (3), then become

$$M\ddot{\mathbf{d}}(t) + C\dot{\mathbf{d}}(t) + K\mathbf{d}(t) = \mathbf{f}(t). \quad (5)$$

Time integration is performed using the Newmark method. The equations solved to obtain displacements, velocities and acceleration at timestep $n+1$ are

$$M\mathbf{a}_{n+1} + C\mathbf{v}_{n+1} + K\mathbf{d}_{n+1} = \mathbf{f}_{n+1}, \quad (6)$$

$$\mathbf{d}_{n+1} = \mathbf{d}_n + \mathbf{v}_{n+1}\Delta t + \frac{\Delta t^2}{2}\left(2\zeta\mathbf{a}_{n+1} + (1-2\zeta)\mathbf{a}_n\right), \quad (7)$$

$$\mathbf{v}_{n+1} = \mathbf{v}_n + \Delta t\left(\gamma\mathbf{a}_{n+1} + (1-\gamma)\mathbf{a}_n\right). \quad (8)$$

The values of γ and ζ are chosen to be $\frac{1}{2}$ and $\frac{1}{4}$ respectively. For this choice of γ ad ζ, the method is second order, unconditionally stable and non-dissipative. For extremely thin materials, 3D solid elements lead to slow convergence of iterative methods used to solve the implicit equations. For the simulations at two Re_τ considered, the Newmark method but with mode superposition time integration (Hughes, 2012) instead of Eqn. (6) is used to obtain the dynamic response.

Implementation

An in-house parallel unstructured finite element solver was developed to solve the above equations. The solver uses in-house parallel sparse matrix storage and operations to effciently assemble matrices of higher order elements and perform operations like matrix-vector multiplications. It supports multiple data structures like cell-based, face-based and node-based under a single framework, uses multi-grid preconditioned linear algebra and eigenvalue solvers from the Trilinos (Heroux et al., 2005) linear algebra package, and Parmetis (Karypis et al., 1997) for partitioning elements between different processors. Parallel-netCDF (Li et al., 2003) for scalable I/O and 4-types of finite elements are presently implemented: 27-node hexahedral, 8-node hexahedral, 9-node quadrilateral and 4-node quadrilateral elements. In-house MPI (Message Passing Interface) communication modules are developed and tested up to 200,000 processors.

Validation

9-node hexahedral and 27-node hexahedral elements were used for all the below described 2D and 3D validation cases, respectively.
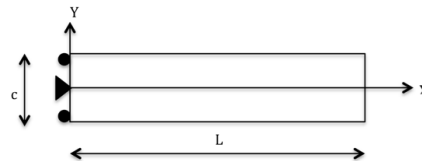

Figure 1: Geometry of 2D cantilever beam.

Fig. 1 shows the geometry of a 2D cantilever beam in plane strain. The boundary conditions are

$$d_1(0,0) = d_2(0,0) = d_1(0,\pm c) = 0, \quad (9)$$

$$h_1(x_1,\pm c) = h_2(x_1,\pm c) = 0, \quad (10)$$

$$h_1(L,x_2) = 0, h_2(L,x_2) = \frac{P}{2I}\left(c^2 - x_2^2\right), \quad (11)$$

$$h_1(0,x_2) = \frac{PLx_2}{I}, h_2(0,x_2) = -\frac{P}{2I}\left(c^2 - x_2^2\right), \quad (12)$$

$$(13)$$

where $h_i(x_1,x_2)$ is the component of surface force at (x_1,x_2) and $I = \frac{2c^3}{3}$. The parameters chosen were $L = 16; c = 2; P = 1$. In each direction, 32 9-node quadrilateral elements were used. From Tab. 1, it can be seen that the numerically obtained tip deflection is in good agreement with the analytical solution for the tip deflection of cantilever beam.

Table 1: Comparison of numerical result with analytical solution for tip deflection of cantilever beam.

Poisson's ratio	Analytical	Numerical
0.3	244.14	244.13
0.499	205.74	205.74
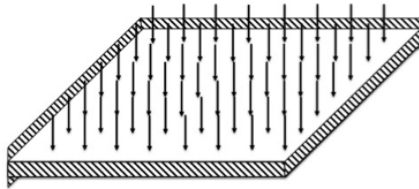
Figure 2: Geometry of 3D clamped plate.

Table 2: Comparison of non-dimensional numerical plate center displacement $\frac{w}{D/(qL^4)}10^3$ with Taylor and Govindjee (2004).

Number of dofs	Reference	Numerical
729	1.27	0.9
2601	1.27	1.18
9801	1.27	1.24
38025	1.27	1.26
17.3×10^6	1.27	1.27

Fig. 2 shows a clamped square plate with uniform pressure loading q. The obtained non-dimensional plate center displacement $\frac{w}{D/(qL^4)}10^3$ is compared to the reference result of Taylor and Govindjee (2004). w is the plate center displacement, D is the plate bending stiffness, q is the uniformly distributed pressure on the plate and L is the length of side of the square plate. The plate bending stiffness $D = \frac{Eh^3}{12(1-v^2)}$ where E is the Young's modulus, h is the plate thickness and v is the poisson's ratio. Tab. 2 shows good agreement and convergence with increase in number of degrees of freedom. Note that the reference results of Taylor and Govindjee (2004) used Poisson-Kirchoff plate theory equations whereas we use 3D elasticity equations without thin plate theory assumptions.

Tab. 3 shows the comparison of computed eigenvalues of first 5 modes of a clamped square plate to the reference results compiled by Leissa (1969). 32 27-node hexahedral elements were used in the axes directions parallel to the plane of the plate and 1 element was used along the plate thickness. Good agreement is seen in the numerically computed eigenvalues.

Table 3: Comparison of non-dimensional numerically obtained natural frequencies $\omega_n\sqrt{\frac{\rho h}{D}}L^2$ with Leissa (1969).

Mode	Reference	Numerical
1	36	36.08
2	73.41	73.58
3	73.41	73.58
4	108.3	108.4
5	131.6	131.92

The time accuracy is validated by comparing the result obtained from direct time integration to the analytical result for a sinusoidally varying force vector with component only along the first mode of vibration. The response of such a forcing will also be along the first mode of vibration which can be obtained from the Duhamel integral (Bathe, 2006). Fig. 3 shows the comparison of component of numerically obtained response along the first mode using Newmark method with analytical solution of modal response. The plate dimension and mesh are same as those used in the eigenvalue validation. The nondimensional forcing frequency $\omega\sqrt{\frac{\rho h}{D}}L^2$ is 10.
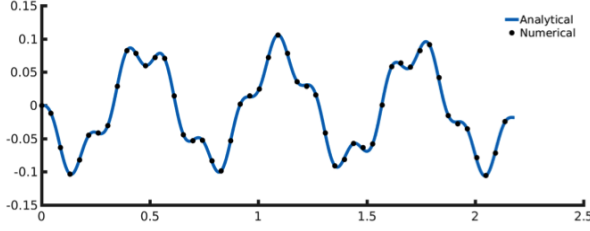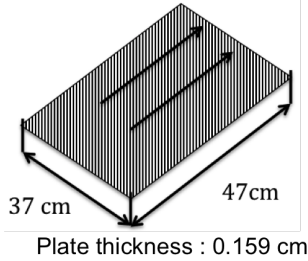
Figure 3: Comparison of numerically obtained component of response along first mode of vibration with analytical result.

SIMULATION DETAILS

We describe the plate geometry, wall-pressure fluctuation generation method and load transfer strategy for the $Re_\tau = 2233$ and $Re_\tau = 180$ cases.

Re_τ=2233

37 cm 47cm

Plate thickness : 0.159 cm

Figure 4: Geometry of the plate used in the experiment by Han et al. (1999)

Table 4: Flow parameters of Han et al. (1999).

Displacement thickness (δ^*)	$0.0024m$
Freestream velocity (U_∞)	$44.7ms^{-1}$

The plate geometry and flow parameters are chosen to match the experiment of Han et al. (1999). Fig. 4 shows the geometry of the plate and Tab. 4 shows the flow parameters of the experiment. The plate material is steel. Calculating wall-shear stress from correlations, Re_τ, boundary layer thickness δ and viscous length scale δ_v are found to be 2233, $1.92 \times 10^{-2}m$ and $8.59 \times 10^{-6}m$, respectively. Note that the viscous length scale is much smaller than the plate thickness. The length of the plate in the streamwise and spanwise directions is 25 to 19 times the boundary layer thickness. The aspect ratio of the plate is approximately 300.

Synthetic space-time wall-pressure fluctuations are generated from a given wavenumber-frequency spectrum, assigning random phases for the individual Fourier coefficients. A spatial domain of size L_1^f in the streamwise, L_2^f in the spanwise direction and a total time T^f is chosen. Here, superscript ^{f} denotes quantities used to generate the synthetic forcing. The continuous space-time wall-pressure fluctuation in the chosen spatial and temporal domain is represented as a Fourier interpolant,

$$p(x_1, x_2, t) =$$
$$\sum_{l_1=-N_1/2}^{N_1/2-1} \sum_{l_2=-N_2/2}^{N_2/2-1} \sum_{-l_3=N_3/2}^{N_3/2-1} \hat{p}_{l_1,l_2,l_3} e^{ik_{l_1}x_1 + ik_{l_2}x_2 + i\omega_{l_3}t}, \quad (14)$$

where N_1, N_2 are the number of wavenumbers in space and N_3 is the number of frequencies considered. The wavenumbers k_{l_1}, k_{l_2} and frequency ω_{l_3} are defined as $k_{l_1} = \frac{2\pi l_1}{L_1^f}$, $k_{l_2} = \frac{2\pi l_2}{L_2^f}$ and $\omega_{l_3} = \frac{2\pi l_3}{T^f}$ respectively. The Fourier coefficients $\hat{p}_{l_1,l_2,l_3}$ are obtained from a given continuous wavenumber-frequency spectrum $S_{pp}(k_1, k_2, \omega)$ as

$$\hat{p}_{l_1,l_2,l_3} = \sqrt{\frac{2\pi}{L_1^f} \frac{2\pi}{L_2^f} \frac{2\pi}{T^f} S_{pp}(k_{l_1}, k_{l_2}, \omega_{l_3})} e^{i\varphi}, \quad (15)$$

where φ is a random number uniformly distributed between 0 and 2π. The generated space-time wall-pressure fluctuations $p(x_1, x_2, t)$ then have the same spectral features as $S_{pp}(k_1, k_2, \omega)$, but are stochastic due to the randomly assigned phase to each of the Fourier coefficients. The Fourier coefficients are generated only in the right half-plane in wavenumber-frequency space. Real data is ensured by enforcing the other half plane to be conjugates of the generated half plane. Rogallo (1981) used a similiar technique to generate initial conditions for a 3D isotropic turbulence simulation. Maxit (2016) used a similar approach in the frequency domain to generate multiple realizations of the Fourier transform $\hat{p}(x_1, x_2, \omega)$. Here, we generate a single realization of wall-pressure fluctuations using the method described above and compute the response of the plate.

The Corcos (1964) model is used for the two-sided wavenumber frequency spectrum $S_{pp}(k_1, k_2, \omega)$ and Smol'Iakov and Tkachenko (1991) is used for the two-sided power spectrum $F_{pp}(\omega)$ of wall-pressure fluctuation.

$$\frac{F_{pp}(\omega)}{\tau_w^2 \delta^*/U_\infty} = \frac{1}{2} \frac{5.1}{1 + 0.44 \left(\frac{|\omega|\delta^*}{U_\infty}\right)^{7/3}}, \quad (16)$$

$$S_{pp}(k_1, k_2, \omega) = F_{pp}(\omega)*$$
$$\frac{\alpha_1}{\pi} \frac{\alpha_2}{\pi} \frac{|\omega|^2}{U_c^2} \frac{1}{\left(\frac{\alpha_1\omega}{U_c}\right)^2 + \left(\frac{\omega}{U_c} + k_1\right)^2} \frac{1}{\left(\frac{\alpha_2\omega}{U_c}\right)^2 + (k_2)^2}, \quad (17)$$

where $\alpha_1 = 0.11$, $\alpha_2 = 0.7$ and convection velocity U_c is assumed to be $0.89U_\infty$. Note that using the above technique, synthetic wall-pressure fluctuations corressponding to any homogenous wavenumber-frequency spectrum can be generated.

The time span of load generation is chosen to be 840 times the time-period of the first mode of vibration to allow the transient response of the structure to decay. The spatial extents L_1^f, L_2^f are chosen to be 10 times the length of the plate in corressponding directions to incorporate wavelengths in the forcing with dimension larger than the plate in each direction. Note that we only include a specific subset of the entire wavenumber space in our simulations. So, the large levels of Corcos model as wavenumbers tend to 0 are likely not an issue in our simulations. In frequency domain simulations where the cross-spectral density obtained by integrating over entire wavenumber space is used to excite the structure, inclusion of the low wavenumber region of Corcos model leads to larger prediction of the structural response (Hwang and Maidanik, 1990).

10000 frequencies in time and 320 wavenumbers in each spatial direction are used to generate the synthetic wall-pressure fluctuation. A parallel implementation was developed to generate around 1 billion wavenumbers.
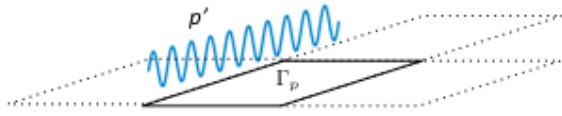
Figure 5: Comparison of length scale of wall-pressure fluctuation to mesh size on the surface of the plate above hydrodynamic coincidence frequency.

The surface pressure enters the system of equations as the force vector in the plate-normal degree of freedom of the ith node through the element integral for the pth element as

$$f_i = \int_{\Gamma^p} N_i(\mathbf{x})p(\mathbf{x},t)d\Gamma. \tag{18}$$

It is well known that above the hydrodynamic coincidence frequency, the length scale of wall-pressure fluctuations becomes smaller than the length scale of the bending structural mode. Therefore, more number of elements are required to resolve the surface pressure than to obtain reasonable response of the structure above the hydrodynamic coincidence frequency. Fig. 5 shows this scenario. Large number of elements just to resolve the surface pressure can be avoided by evaluating the surface integrals in the right hand side of Eqn. 18 to high accuracy using a large number of Gauss-Legendre integration points. However, this method is extremely

expensive for the synthetic wall-pressure fluctuation case as we need to perform approximately a billion additions and multiplications to obtain pressure at a given time for a given quadrature point in an element. We use the fact that the domain is Cartesian and perform L^2 orthogonal projection of sines and cosines in Eqn. 14 onto the space of polynomials of degree 2 using Legendre polynomial basis (Powell, 1981) at a given time. This results in a method where we only need to store 9 coefficients of a 2D Legendre polynomial basis on each element on the plate surface per timestep. The resulting evaluation of the surface integral using the projected Legendre polynomial in place of $p(\mathbf{x},t)$ in Eqn. 18 with 3 quadrature points will give the exact result.

The frequency range of interest in the structural simulation is up to 500 Hz. 32 quad 27-node hexahedral elements are used in each spatial direction with 1 element along the thickness. The mesh resolution was decided so as to sufficiently resolve the mode shapes of natural frequencies that are in the frequency range of interest. The timestep of the simulation is chosen to be $5 \times 10^{-5}s$ to have around 20 points in the time-period of the largest frequency used to generate the pressure fluctuations. Rayleigh damping coefficients were chosen so as to have a loss factor of around 0.003-0.006 in the frequency range of interest. Since the aspect ratio of the plate is around 300, 3D solid elements with direct time integration using Eqn.6 suffered from extremely slow convergence of implicit solver even though multi-grid preconditioned conjugate gradient method was used for the iterative solver. Therefore, we use the modal superposition time integration method (Hughes, 2012). We compute 20 modes of the plate and the force vector at each timestep is projected onto these modes. The resulting decoupled ODEs are integrated using Newmark method to obtain the individual modal response. The total response of the plate is then obtained by summing over the individual modal response.

Re_τ=180

Wall-pressure fluctuations for $Re_\tau = 180$ are generated using DNS of turbulent channel flow. The governing equations are the incompressible Navier-Stokes equations (summation implied on repeated indices),

$$\frac{\partial u_i^f}{\partial x_i} = 0, \tag{19}$$

$$\frac{\partial u_i^f}{\partial t} + \frac{\partial u_i^f u_j^f}{\partial x_j} = -\frac{\partial p^f}{\partial x_i} + \nu\frac{\partial^2 u_i^f}{\partial x_j \partial x_j}, \tag{20}$$

where u_i^f is the fluid velocity, p^f is the fluid pressure and ν is the kinematic viscosity of the fluid. Note that density of the fluid is absorbed in fluid pressure, p^f.

DNS is performed using the finite volume numerical method of Mahesh et al. (2004). The method is discretely kinetic energy conserving in the absence of time discretization error. We use an implicit version of the method using Crank-Nicholson time integration scheme.

All quantities are non-dimensionalized based on channel half height and friction velocity u_τ. The computational domain is a box $2\pi \times 2 \times \pi$ where 2π, 2 and π are lengths in streamwise, wall-normal and spanwise directions respectively. A Cartesian domain of $341 \times 128 \times 207$ control volumes (CVs) is used. A total of 9 million CVs are used on 256 processors to perform the DNS. The timestep used for the simulation is 5×10^{-4} which is in viscous units $0.09\nu/u_\tau^2$. A uniform mesh is used in streamwise and spanwise directions, and a non-uniform mesh is used in the wall-normal direction. The streamwise, spanwise, near wall and channel center spacing in the wall-normal direction is 3.3, 2.73, 0.8 and 4.6 in wall units respectively.

The bottom wall of the channel is assumed to be elastic. Therefore, the plate length (in fluid non-dimensional units) is taken to be 2π in the streamwise and π in the spanwise directions. The thickness of the plate is chosen to be $\pi/100$. The wall-pressure fluctuations obtained from DNS is saved for a total of 17 units with time separation of 5×10^{-4} and then transferred to the structure. Two materials of the plate are considered: steel and POM polyacetate material. The range of frequencies where the wall-pressure power spectrum has reasonable levels ($0\text{-}250u_\tau/\delta$) contains around 2 natural frequencies for the steel plate and around 17 natural frequencies for the POM polyacetate plate. Similar to the $Re_\tau = 2233$ simulation, the structural mesh need not be designed to resolve the surface pressure, but instead can be chosen to resolve the mode shapes. The following load transfer methodology is used to transfer the surface pressure forces from the fine fluid mesh to a coarse solid mesh.
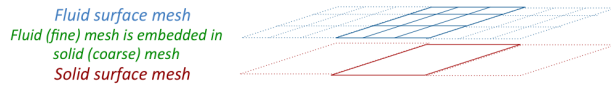
Figure 6: Fine fluid mesh embeddded in coarse solid mesh.

We assume the fluid mesh to be finer and embedded in a surface mesh as in Fig. 6, i.e. multiple fluid mesh element faces can be combined to form a single solid element face. Even though this embedding of meshes may not be possible for extremely complex geometries, we can take advantage of this for the current load transfer problem. The spatial variation of pressure fluctuations is assumed to be piecewise constant on the fluid surface mesh. The load is first computed on the

nodes of the fine fluid surface mesh and then transfered to the coarse solid mesh. Since the surface meshes are embedded, we can write the shape function N_i^s associated with the ith node of the solid mesh as a linear combination of the shape function N_j^f associated with the nodes of the fluid mesh as

$$N_i^s(\mathbf{x}) = \sum_{j=1}^{n^f} \gamma_{ij} N_j^f(\mathbf{x}) \quad ; i = 1, \ldots, n^s, \qquad (21)$$

where n^f and n^s are the number of nodes on the fluid and solid surface mesh respectively. Then, the force on the plate normal degree of freedom associated with the ith node of solid mesh can be obtained as a linear combination of the nodal forces on the fine fluid mesh as

$$\int_{\Gamma_p} N_i^s(\mathbf{x}) p(\mathbf{x},t) d\mathbf{x} = \sum_{j=1}^{n^f} \gamma_{ij} \int_{\Gamma_p} N_j^f(\mathbf{x}) p(\mathbf{x},t) d\mathbf{x}$$

$$i = 1, \ldots, n^s. \qquad (22)$$

The surface forces evaluated from Eqn. 22 are exact given the piecewise constant representation of surface pressure on the fluid mesh. Also, this load transfer framework is implemented in parallel for simulations that will involve surface pressure described on very fine fluid meshes. This method can be shown to be equivalent to the optimal Mortar method of solution transfer between different meshes (Farhat et al., 1998).

Table 5: Material properties of steel and POM polyacetate plates.

Property	Stainless steel	POM polyacetate
Young's modulus	$200GPa$	$3GPa$
Density	$8000kgm^{-3}$	$1480kgm^{-3}$
Poisson's ratio	0.3	0.35
Loss factor	0.002-0.01	0.0013-0.008

The solid equations are non-dimensionalized based on ρ^f, u_τ and channel half height. Since we need physical values ρ^f and u_τ to compute non-dimensional solid density and Young's modulus, ρ^f is chosen to be that of air and u_τ is set to $1ms^{-1}$ for convenience. The material properties of the two plate materials are shown in Tab. 5. Similar to the $Re_\tau = 2233$ case, mode superposition time integration with 20 modes is used. The timestep is chosen to be the same as that of the DNS simulation. We use 27-node hexahedral solid elements for the plate. The solid surface is obtained by coarsening the fluid surface mesh by a factor of 5. 68 elements were used in the streamwise and 40 elements were used in the spanwise direction with 1 element along the plate thickness.
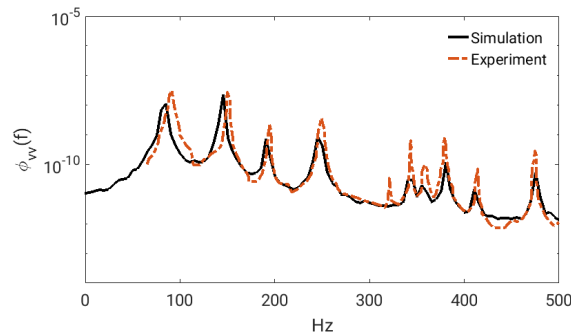
RESULTS

$Re_\tau=2233$
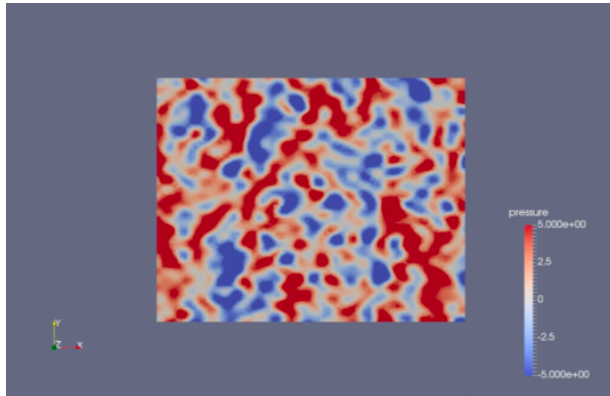
Figure 7: Sample instantaneous spatial variation of synthetic wall-pressure field.
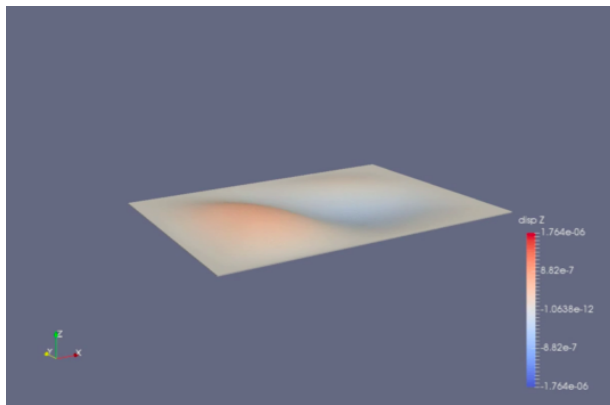
Figure 8: Sample instantaneous deformation (scaled 50000 times) of the plate.


Figure 9: Comparison of the plate velocity spectra at a point 15cm from the plate's left edge and 12cm from its bottom edge.

Figs. 7 and 8 show the instantaneous wall-presure fluctuation field and response of the plate respectively. The ratio of bending wave speeds (c_m) of the modes of vibration with convection velocity (U_c) in the frequency range considered varies from 0.22-0.84. The rms displacement and velocity of plate center are $0.5\delta_v$ and $0.001u_\tau$ respectively. These rms values show that the plate vibration is mostly confined to the viscous sublayer of the boundary layer and is too small to affect the turbulent boundary layer, thereby justifying one-way coupled simulations where the loads from a rigid wall are used to excite the flexible structure. Also, the non-dimensional first natural frequency of the plate non-dimensionalized with boundary layer quantities δ, u_τ is 5.893. This shows that the plate vibration time scale is of the same order as the boundary layer time scale.

Fig. 9 compares the plate velocity spectra at a point 15cm from the plate's left edge and 12cm from the bottom edge of the plate to measured experimental data of Han et al. (1999). From Fig. 9, it can be seen that the numerically computed plate velocity spectrum agrees better for frequencies lower than 300Hz than for frequencies larger than 300Hz. This will be investigated in further work by performing simulations with higher number of elements.
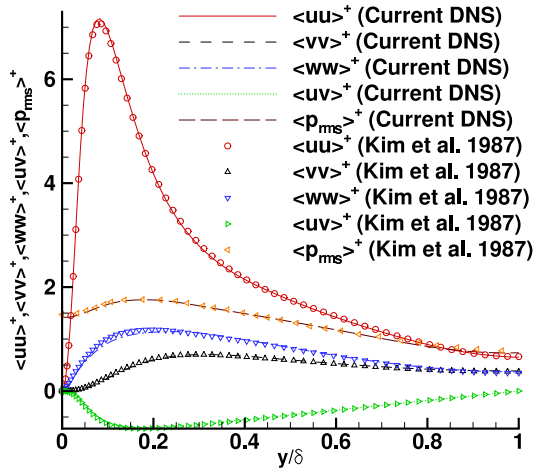
$Re_\tau=180$

Figs. 10 and Fig. 11 compare mean and fluctuation statistics of the velocity and pressure fields from the current DNS to that of Kim et al. (1987) respectively. Good agreement is observed.
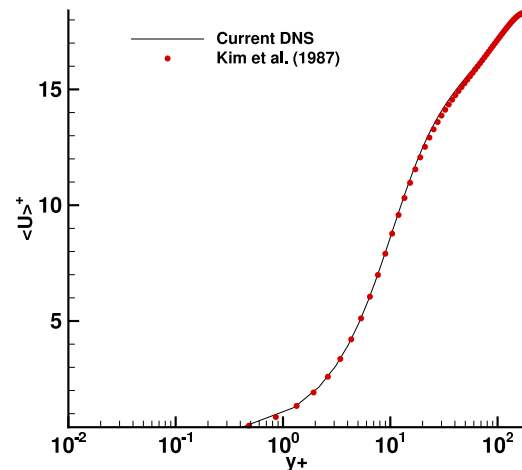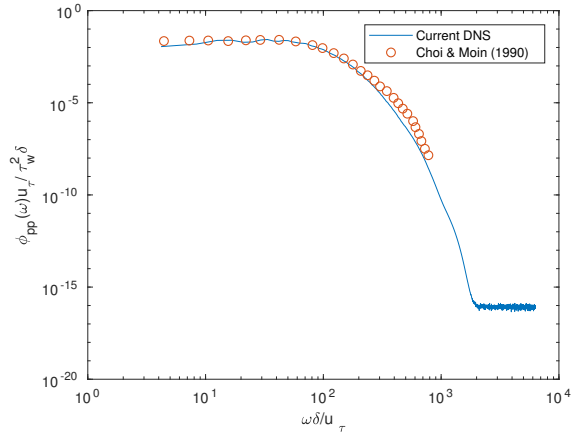

**Figure 10:** Comparison of mean velocity profile with DNS of Kim et al. (1987).

Figure 11: Comparison of Reynolds stress and r.m.s. pressure fluctuation profiles with DNS of Kim et al. (1987). Superscript $^+$ denotes quantities in wall units.
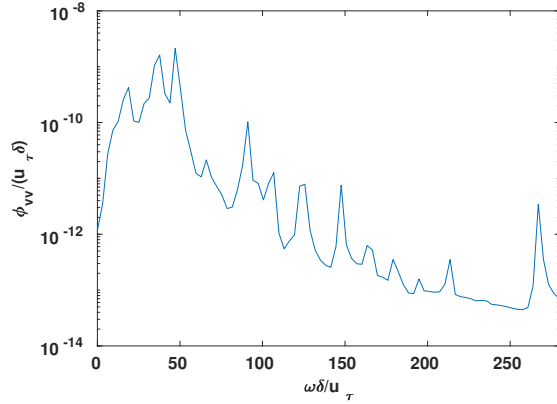

Figure 12: One-sided power spectrum of wall-pressure fluctuations.

Table 6: RMS displacement and wall-normal velocity of the plate at (-1.059,-0.531) in wall units. (Plate center is at (0,0))

Property	Steel	POM polyacetate
$\frac{<d^2>^{1/2}}{\delta_v}$	2.61×10^{-3}	0.252
$\frac{<v^2>^{1/2}}{u_\tau}$	1.34×10^{-6}	2.21×10^{-4}
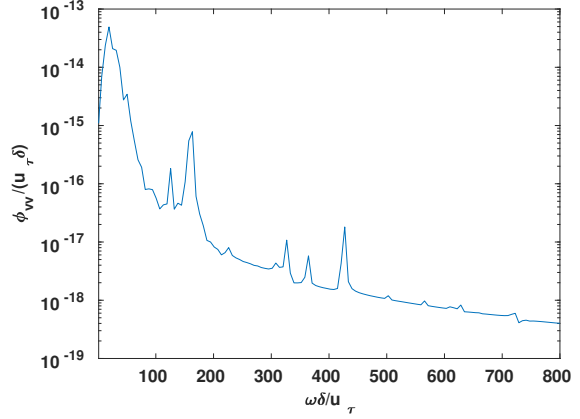
Figure 13: Velocity power spectra at (-1.059,-0.531) for steel plate. (Plate center is at (0,0).)

Figure 14: Velocity power spectra at (-1.059,-0.531) for POM polyacetate plate. (Plate center is at (0,0).)

Fig. 12 shows the comparison of one-sided power spectral density of wall-pressure with the DNS results of Choi and Moin (1990). The total time length of the samples and the time separation between the samples for the computation of one-sided power spectral density of wall-pressure is $15\delta/u_\tau$ and $5 \times 10^{-4}\delta/u_\tau$ respectively. We use Hanning window with 50% overlap to avoid leakage of the power spectra and increase convergence. Also, a factor of 8/3 has been multiplied to the obtained power spectral density to correct the estimates following the application of Hanning window (Bendat and Piersol, 2011). Good agreement is observed in Fig. 12.

With the plate center fixed at (0,0), the plate wall-normal displacement and velocity are probed at (-1.059,-0.531) for both plate materials. Fig. 13 and 14 show the computed point velocity spectra at the probe location. In the frequency range with values of $\omega\delta/u_\tau$ between 0 and 250, the spectral levels shown in Fig.

12 have reasonable magnitude. For the steel plate, only two natural frequencies are present in this range, whereas around 17 out of the 20 considered mode shapes are present for the polyacetate plate. For the steel plate, the first two non-dimensional natural frequencies ($\omega_n \delta / u_\tau$) are approximately around 126 and 160 which corresspond to the peaks observed in the same location in Fig. 13. These two frequencies are located in the roll-off region of the wall-pressure spectrum. However, for the POM polyacetate plate, several natural frequencies are located in the frequency range $\omega \delta / u_\tau$ of 0 to 100 where the power spectrum has a constant relatively large magnitude. The peak in the plate velocity spectra at $\omega \delta / u_\tau = 36$ and $\omega \delta / u_\tau = 46$ in Fig. 14 corresspond to the first two natural frequencies of the POM polyacetate plate. We will perform more simulations in future for the POM polyacetate plate with larger number of elements and with a higher number of mode shapes.

Table 6 shows the rms values of dispacement and velocity of the two plate materials considered at the probe location. It can be seen that rms values are very small in wall units, thereby justifying one-way coupled simulations. Also, the rms displacement and velocity of steel plate is two orders of magnitude smaller than that of POM polyacetate plates.

CONCLUSION

In this paper, we described the development and validation of a parallel in-house finite element structural solver. The structural solver is then used to obtain plate response at $Re_\tau = 2233$ and $Re_\tau = 180$. A methodology to generate homogenous synthetic space-time wall-pressure fluctuations from a given wavenumber frequency and power spectrum is discussed. An efficient and accurate surface force computation strategy for surface pressure described using a large number of Fourier coefficients based on L^2 orthogonal projection is presented which avoids the need to refine the structural mesh to capture the fine spatial variation of surface pressure above the hydrodynamic coincidence frequency. This technique can also be used in frequency domain FEM calculations. Plate response at $Re_\tau = 2233$ is then computed from the generated synthetic wall-pressure fluctuations and compared with the experimental results of Han et al. (1999). Wall-pressure fluctuations at $Re_\tau = 180$ are generated using DNS of turbulent channel flow. An optimal load transfer method is described to compute the forces on the structural mesh when the fine fluid surface mesh is embedded in the coarse solid surface mesh. The response of steel and POM polyacetate plates is obtained using the DNS wall-pressure fluctuations at $Re_\tau = 180$ and compared. The rms values of velocity and displacement computed at a point on the POM polyacetate plate is around two orders of magnitude larger than that of steel plate with same dimensions.

REFERENCES

Bathe, K. J. Finite element procedures. Klaus-Jurgen Bathe, 2006.

Bendat, J. S. and Piersol, A. G. Random data: analysis and measurement procedures, volume 729. John Wiley & Sons, 2011.

Blake, W. K. "Turbulent boundary-layer wall-pressure fluctuations on smooth and rough walls". Journal of Fluid Mechanics, 44(4):637–660, 1970.

Blake, W. K. Mechanics of Flow-Induced Sound and Vibration, Volume 1 and 2. Academic Press, 2017.

Brenner, S. and Scott, R. The mathematical theory of finite element methods, volume 15. Springer Science & Business Media, 2007.

Bull, M. K. "Wall-pressure fluctuations associated with subsonic turbulent boundary layer flow". Journal of Fluid Mechanics, 28(4):719–754, 1967.

Bull, M. K. "Wall-pressure fluctuations beneath turbulent boundary layers: some reflections on forty years of research". Journal of Sound and Vibration, 190(3): 299–315, 1996.

Caiazzo, A. and Desmet, W. "A generalized Corcos model for modelling turbulent boundary layer wall pressure fluctuations". Journal of Sound and Vibration, 372: 192–210, 2016.

Chang, P.A., Ebert, M., Young, Y. L., Liu, Z., Mahesh, K., Jang, H., and Shearer, M. "Propeller forces and structural response due to crashback". In 27th Symposium on Naval Hydrodynamics, Seoul, Korea, Oct, pages 5–10, 2008.

Chase, D. M. "Modeling the wavevector-frequency spectrum of turbulent boundary layer wall pressure". Journal of Sound and Vibration, 70(1):29–67, 1980.

Choi, H. and Moin, P. "On the space-time characteristics of wall-pressure fluctuations". Physics of Fluids A: Fluid Dynamics, 2(8):1450–1460, 1990.

Ciappi, E., Magionesi, F., De Rosa, S., and Franco, F. "Hydrodynamic and hydroelastic analyses of a plate excited by the turbulent boundary layer". Journal of Fluids and Structures, 25(2):321–342, 2009.

Ciappi, E., Magionesi, F., De Rosa, S., and Franco, F. "Analysis of the scaling laws for the turbulence driven panel responses". Journal of Fluids and Structures, 32: 90–103, 2012.

Ciappi, E., De Rosa, S., and Franco, F. "Dimensionless representations of the interaction between turbulent boundary layer and elastic plates". In Flinovia-Flow Induced Noise and Vibration Issues and Aspects, pages 279–298. Springer, 2015.

Corcos, G. M. "The structure of the turbulent pressure field in boundary-layer flows". Journal of Fluid Mechanics, 18(3):353–378, 1964.

Elishakoff, I. Probabilistic Methods in the Theory of Structures: Strength of Materials, Random Vibrations, and Random Buckling. World Scientific, 1983.

Farabee, T. M. and Casarella, M. J. "Spectral features of wall pressure fluctuations beneath turbulent boundary layers". Physics of Fluids A: Fluid Dynamics, 3(10): 2410–2420, 1991.

Farhat, C., Lesoinne, M., and Le Tallec, P. "Load and motion transfer algorithms for fluid/structure interaction problems with non-matching discrete interfaces: Momentum and energy conservation, optimal discretization and application to aeroelasticity". Computer Methods in Applied Mechanics and Engineering, 157(1-2):95–114, 1998.

Goody, M. "Empirical spectral model of surface pressure fluctuations". AIAA Journal, 42(9):1788–1794, 2004.

Graham, W. R. "A comparison of models for the wavenumber–frequency spectrum of turbulent boundary layer pressures". Journal of Sound and Vibration, 206(4):541–565, 1997.

Hambric, S. A., Hwang, Y. F., and Bonness, W. K. "Vibrations of plates with clamped and free edges excited by low-speed turbulent boundary layer flow". Journal of Fluids and Structures, 19(1):93–110, 2004.

Hambric, S. A., Shaw, M., Campbell, R. L., and Conlon, S. C. "Calculating structural vibration and stress from turbulent flow induced forces". In Flinovia-Flow Induced Noise and Vibration Issues and Aspects, pages 343–356. Springer, 2015.

Han, F., Bernhard, R. J., and Mongeau, L. G. "Prediction of flow-induced structural vibration and sound radiation using energy flow analysis". Journal of Sound and Vibration, 227(4):685–709, 1999.

Heroux, M. A., Bartlett, R. A., Howle, V. E., Hoekstra, R. J., Hu, J. J., Kolda, T. G., Lehoucq, R. B., Long, K. R., Pawlowski, , R. P., Phipps, T., E., and Salinger, A. G. "An overview of the Trilinos project". ACM Transactions on Mathematical Software (TOMS), 31 (3):397–423, 2005.

Hu, N., Reiche, N., and Ewert, R. "Simulation of turbulent boundary layer wall pressure fluctuations via poisson equation and synthetic turbulence". Journal of Fluid Mechanics, 826:421–454, 2017.

Hu, Z., Morfey, C. L., and Sandham, N. D. "Wall pressure and shear stress spectra from direct simulations of channel flow". AIAA Journal, 44(7):1541–1549, 2006.

Hughes, T. J. R. The finite element method: linear static and dynamic finite element analysis. Courier Corporation, 2012.

Hwang, Y. F. "A discrete model of turbulence loading function for computation of flow-induced vibration and noise". In Proceedings of the ASME International Mechanical Engineering Congress and Exposition, Anaheim, CA, 1998.

Hwang, Y. F. and Maidanik, G. "A wavenumber analysis of the coupling of a structural mode and flow turbulence". Journal of Sound and Vibration, 142(1): 135–152, 1990.

Hwang, Y. F., Bonness, W. K., and Hambric, S. A. "Comparison of semi-empirical models for turbulent boundary layer wall pressure spectra". Journal of Sound and Vibration, 319(1-2):199–217, 2009.

Karypis, G., Schloegel, K., and Kumar, V. "Parmetis: Parallel graph partitioning and sparse matrix ordering library". Version 1.0, Dept. of Computer Science, University of Minnesota, page 22, 1997.

Kim, J. "On the structure of pressure fluctuations in simulated turbulent channel flow". Journal of Fluid Mechanics, 205:421–451, 1989.

Kim, J., Moin, P., and Moser, R. "Turbulence statistics in fully developed channel flow at low Reynolds number". Journal of Fluid Mechanics, 177:133–166, 1987.

Lee, Y. T., Blake, W. K., and Farabee, T. M. "Modeling of wall pressure fluctuations based on time mean flow field". Journal of Fluids Engineering, 127(2):233–240, 2005.

Leissa, A. W. "Vibration of plates". Technical report, Ohio State University, Columbus, Ohio, 1969.

Li, J., Liao, W. K., Choudhary, A., Ross, , R., , Thakur, R., Gropp, W., Latham, R., Siegel, A., Gallagher, B., and Zingale, M. "Parallel netcdf: A high-performance scientific i/o interface". In Supercomputing, 2003 ACM/IEEE Conference, pages 39–39. IEEE, 2003.

Mahesh, K., Constantinescu, G., and Moin, P. "A numerical method for large-eddy simulation in complex geometries". Journal of Computational Physics, 197(1):215–240, 2004.

Mahesh, K., Kumar, P., Gnanaskandan, A., and Nitzkorski, Z. "LES applied to ship research". Journal of Ship Research, 59(4):238–245, 2015.

Maxit, L. "Simulation of the pressure field beneath a turbulent boundary layer using realizations of uncorrelated wall plane waves". The Journal of the Acoustical Society of America, 140(2):1268–1285, 2016.

Na, Y. and Moin, P. "The structure of wall-pressure fluctuations in turbulent boundary layers with adverse pressure gradient and separation". Journal of Fluid Mechanics, 377:347–373, 1998.

Panton, R. L. and Linebarger, J. H. "Wall pressure spectra calculations for equilibrium boundary layers". Journal of Fluid Mechanics, 65(2):261–287, 1974.

Peltier, L. J. and Hambric, S. A. "Estimating turbulent-boundary-layer wall-pressure spectra from CFD RANS solutions". Journal of Fluids and Structures, 23(6):920–937, 2007.

Powell, M. J. D. Approximation theory and methods. Cambridge university press, 1981.

Rogallo, R. S. "Numerical experiments in homogeneous turbulence". NASA TM-81315, 1981.

Schäfer, F., Müller, S., Uffinger, T., Becker, S., Grabinger, J., and Kaltenbacher, M. "Fluid-structure-acoustic interaction of the flow past a thin flexible structure". AIAA Journal, 48(4):738–748, 2010.

Sillero, J. A., Jiménez, J., and Moser, R. D. "One-point statistics for turbulent wall-bounded flows at Reynolds numbers up to $\delta+\approx 2000$". Physics of Fluids, 25(10): 105102, 2013.

Smol'Iakov, A. V. and Tkachenko, V. M. "Models of a field of pseudoacoustic turbulent wall pressures and experimental data". Akusticheskii Zhurnal, 37: 1199–1207, 1991.

Taylor, R. L. and Govindjee, S. "Solution of clamped rectangular plate problems". International Journal for Numerical Methods in Biomedical Engineering, 20 (10):757–765, 2004.

Willmarth, W. W. "Pressure fluctuations beneath turbulent boundary layers". Annual Review of Fluid Mechanics, 7(1):13–36, 1975.

Willmarth, W. W. and Wooldridge, C. E. "Measurements of the fluctuating pressure at the wall beneath a thick turbulent boundary layer". Journal of Fluid Mechanics, 14(2):187–210, 1962.